Draft
Submitted ApJ
4/4/03.

Where was the Iron Synthesized in Cassiopeia A?

Una Hwang[1] & J. Martin Laming[2]

ABSTRACT

We investigate the properties of Fe-rich knots on the east limb of the Cassiopeia A supernova remnant observed with Chandra/ACIS. Using analysis methods developed in a companion paper, we constrain the ejecta density profile and the Lagrangian mass coordinates of the knots from their fitted ionization age and electron temperature. Fe-rich knots which also have strong emission from Si, S, Ar, and Ca are clustered around mass coordinates $q \simeq 0.35 - 0.4$ in the shocked ejecta of mass $2M_\odot$; this places them $0.7-0.8M_\odot$ out from the center (or $2-2.1M_\odot$, allowing for the mass of a compact object). We also find an Fe clump that is evidently devoid of line emission from lower mass elements, as would be expected for a region that had undergone α-rich freeze out. This clump has a similar mass coordinate to the other Fe knots.

1. Introduction

Cassiopeia A is the only supernova remnant for which decays of the important radioactive nucleus ^{44}Ti have been confirmed by observation of γ ray line emission from both of its decay products, ^{44}Sc and ^{44}Ca (Iyudin et al. 1994, 1997; Vink et al. 2001; Vink & Laming 2003). The ^{44}Ti is almost uniquely produced in the explosive Si burning condition known as α-rich freeze out, wherein Si burns at high temperature and relatively low density. It occurs

[1]Goddard Space Flight Center and University of Maryland

hwang@orfeo.gsfc.nasa.gov

[2]Code 7674L, Naval Research Laboratory, Washington DC 20375

jlaming@ssd5.nrl.navy.mil

in the innermost ejecta and is highly sensitive to the explosion details and the position of the mass cut for the formation of a neutron star or black hole. The location of α-rich freeze out is thus of great interest and importance to theoretical progress on the mechanisms by which core-collapse supernovae explode, but direct imaging of the hard X-rays or γ-rays from the ^{44}Ti decay is technically very difficult at the necessary spatial resolution. An attractive alternative approach, recently proposed by Silver et al. (2001), is to use a very high spectral resolution calorimeter to search for Doppler structure in the ^{44}Sc emission lines at 67.9 and 78.4 keV, but this also must await the development of the required instrumentation.

A different approach explored in this paper depends on the nucleosynthesis signature of α-rich freeze out. The usual explosive Si burning produces mainly ^{56}Fe (originally as ^{56}Ni, which decays radioactively), along with Si, S, Ar, and Ca. Because α-rich freeze out happens very fast at low density and high temperature, the burning products, apart from ^{44}Ti and a small amount of ^{4}He, are almost exclusively ^{56}Fe. The principal reason for this difference is that the low density suppresses the $3\alpha \rightarrow ^{12}$C reaction, to shift the nuclear statistical equilibrium (or quasi-equilibrium) to heavier nuclei around the iron peak (Woosley & Hoffman 1991; Arnett 1996; The et al. 1998). Lighter nuclei, including ^{44}Ti, are formed in small amounts towards the end of the freeze out by α captures. The X-ray spectrum of a freeze out region should thus show emission lines only from Fe. It is our purpose in this paper to locate such region(s) in the extant Chandra observations of Cas A, and to characterize them in terms of their temperatures and ionization ages. By using a model for the supernova remnant hydrodynamics, we then place limits on the Lagrangian mass coordinates where such burning took place.

2. The Structure of Cassiopeia A

In a companion paper (Laming & Hwang 2003, Paper I), we use a new analysis approach to quantify asymmetries in the X-ray emitting ejecta of Cas A. Spectra from the Chandra X-ray Observatory are used to obtain temperatures and ionization ages for ejecta knots, and these measured quantities are then compared to the predictions of model calculations that incorporate the basic relevant atomic and plasma physics and follow the dynamics of a remnant expanding into a circumstellar environment. For ejecta with a radial density structure described by a power-law envelope surrounding a constant density core, this approach allows us to deduce the slope of the ejecta envelope in each of the azimuthal directions we examine. By forcing the models to share a common core ejecta density, and fixing the forward shock radius in the models to match the observed average X-ray radius, we may interpret the inferred variations in the ejecta envelope slope as due to variations in the locally de-

posited explosion energy. The variations we deduce are modest, at about a factor of two, with shallower slopes (and higher inferred explosion energy) at the base of the ejecta jet in the northeast than in the east or northwest. A factor of two asymmetry is at the low end predicted by models, but at present, it is not possible on the basis of ejecta density and energy asymmetries alone to distinguish between the two basic mechanisms to produce asymmetries, namely rotation of the progenitor or a jet-induced explosion (Fryer & Heger 2001; Fryer & Warren 2003; Khokhlov et al. 1999).

The method of Laming & Hwang (2003) makes the assumptions that Cas A is propagating into a circumstellar environment (i.e., the dependence of the density ρ on the radius r is $\rho \propto r^{-2}$) and that the spectra of individual knots can be modelled with a single temperature and ionization age. There is substantial evidence that supports a circumstellar environment for Cas A. Slow-moving, N-rich optically emitting knots are generally accepted to be relics of the progenitor's mass loss, and a wind circumstellar density profile is far more viable than a constant density environment in light of such observations as the relative radii of the reverse and forward shocks (Gotthelf et al. 2001), the X-ray expansion rate (DeLaney & Rudnick 2003), and also in terms of the implied ejecta mass and the production of nonthermal X-ray emission via lower hybrid waves (Laming 2001a,b; Vink & Laming 2003). A single temperature and ionization age may plausibly be used to model the spectrum of the knots, because they have angular scales of $\sim 1''$ corresponding to $\sim 5 \times 10^{16}$ cm (at a distance of 3.4 kpc); a 1000 km/s reverse shock can thus traverse the knot in just 20 years, which is much shorter than the timescale for the dynamical evolution of the remnant. These points are further discussed in Laming & Hwang (2003).

Early Chandra observations showed that the Fe emission in Cas A is dominant in the faint region outside the bright ejecta shell in the east (Hughes et al. 2000; Hwang, Holt, & Petre 2000). Typical surface brightness enhancements for the Fe features are only a factor of a few above their immediate surroundings. The Fe-rich knots will be shown here (also see Laming & Hwang 2003) to require higher ionization ages than the O/Si knots,[3] implying either a high density or an early shock time. Because knots and clouds with large density enhancements (or deficits) are subject to a number of hydrodynamical instabilities that act to destroy the knot within a few shock crossing timescales (Klein, McKee & Colella 1994; Klein et al. 2003; Wang & Chevalier 2001; Poludnenko, Frank, & Blackman 2001; McKee & Cowie 1975), such knots are not expected to survive longer than several tens of years. We believe that early shock times and very modest (or no) density enhancements are the most consistent explanation for the Fe knots, accounting for their observed spectral characteristics

[3]The ionization age $n_e t$ is defined as the product of electron density and the time since the plasma was shock-heated.

while allowing for their low surface brightness, and making it plausible for the shocked knots to survive until the present day. The low surface brightness enhancement that is observed could be effected, not by increased density, by the much higher emissivity of Fe-rich plasma compared to solar abundance plasma at the same temperature and ionization age.

3. Data Reduction and Analysis

For the imaging analysis and most of the spectral analysis, we use the same January 2000 observation of Cas A with the Advanced CCD Imaging Spectrometer (ACIS) on the Chandra Observatory that was used by Laming & Hwang (2003), and is described therein. For one interesting and faint region, however, we also use data from a second epoch observation of Cas A taken two years after the first, in January 2002. Both observations are of 50 ks duration and were taken with the same instrument in the same configuration. The spectra from the two epochs are fitted jointly, rather than being added into a single spectrum, because of the time-varying response of the ACIS detector. These effects include time-dependent changes in the gain and resolution caused by charge-transfer inefficiency, and particularly, the temporally increasing absorption of soft X-rays (with energies below about 1 keV) by contaminants on the detector surface. This detector absorption is modelled by ACISABS in the XSPEC X-ray spectral fitting program, with the number of days elapsed from launch to the observation specified.

3.1. Identification of Fe-rich Regions

In searching for regions dominated by Fe ejecta, we are aided by the combined spectral and imaging capabilities of the Chandra Observatory. X-ray images of Cas A in its prominent Fe K blend (energy $\sim$6.7 keV) show that this emission is distributed in three primary regions—to the southeast, northwest, and west (Hwang, Holt, & Petre 2000; Willingale et al. 2002). The western region suffers from a higher interstellar column density that attenuates the low energy X-ray emission, so that the Fe L emission (energies near 1 keV) is prominent only in the southeast and northwest. The southeast region is of particular interest in that the Fe emission here is located exterior to that of Si, suggesting a large-scale convective overturn of the ejecta layers (Hughes et al. 2000). In the northwest, the Fe emission coexists with emission from Si and other intermediate mass elements, at least in projection, but Doppler measurements made with XMM (Willingale et al. 2002) indicate larger line-of-sight velocities for Fe that imply that the Fe emitting region is actually kinematically and spatially distinct from that of other elements such as Si. Overturn of the Fe layers thus appears to

have occured in the northwest as well as in the southeast, except that it is not viewed in a favorable orientation.

The left panel of Figure 1 shows the southeast region of Cas A. The blast shocked material may be seen in places as faint, thin arcs at the outer boundary of the remnant, while the ejecta make up the bright irregular ring of emission. The faint, linear filaments of the ejecta "jet", which are also seen optically, can be seen towards the top of the image. East of the bright ejecta ridge running southward from the jet, the fainter ejecta emission is largely Fe-rich. The Fe features have various morphologies ranging from compact knots to elongated knots, to relatively diffuse features.

Regions of the remnant that have strong line emission relative to the underlying continuum may be selected independently of surface brightness by forming an estimate of the line-to-continuum ratio at each position. For the Fe L blends, it is difficult to reliably subtract the true continuum, but we have made a rough estimate in order to identify the Fe-richest regions. The right panel of Figure 1 shows the Chandra image in the Fe L blends overlaid with smoothed contours showing the regions with prominent Fe line-to-continuum ratios. It is seen that the strongest Fe line emission comes from a line of compact knots running due east at DEC $\sim 58°46'40''$ as well as from diffuse regions of relatively low surface brightness about an arcminute to the south. These are thus our primary target regions to search for sites of α-rich freeze out. The spectral extraction regions (generally a few arcseconds in extent) are shown in the left panel of Figure 1.

The level of surface brightness contrast seen for the Fe and Si features is illustrated in Figure 2. The first panel shows a vertical profile through two representative Fe knots (numbered 13 and 14, starting with 10 closest to the center[4]). The knots are seen to sit on a shelf of emission that rises above the general background. The second panel shows a vertical profile through the larger diffuse Fe-rich cloud in Figure 1. It too sits on a shelf of even fainter emission, but the surface brightness contrasts are seen to be significantly lower than for the other Fe-rich knots. In comparison, the Si rich emission features are much brighter than the background or the Fe rich emission, as seen in the last two panels of Figure 2.

---

[4]The radial series of knots is the extension eastward of the east series of knots studies in Laming & Hwang (2003); the numbering scheme here thus starts where that series left off at A10, increasing eastward to A17.

3.2. X-ray Spectral Analysis

We carried out spectral fits for the regions indicated in Figure 1 with a model characterized by a single temperature and single ionization age, wherein the lightest element included is O, and O provides the bulk of the continuum. This is consistent with the expectation that O is the primary constituent of the ejecta in Cas A, and follows the approach first adopted by Vink, Kaastra, & Bleeker (1996) for modelling the X-ray ejecta spectra with an O-rich plasma. As Fe is by far the most prominent feature in all of these spectra, we also consider models where Si, rather than O, is the lightest element. The background spectrum is generally taken from positions well off the source. For the Fe/Si ejecta models, we also take a more localized background from low-surface brightness regions in the vicinity of the Fe knots. The results of all these fits are summarized in Table 1, and the fits for a typical knot are shown in Figure 3.

For the Fe knots (A series), the fits are generally better with O ejecta than Si ejecta using the standard background, but in both cases, the ionization ages are $\sim 10^{11}$ cm^{-3}s or higher. Compared to the fits with Fe/Si continuum, the O continuum fits give temperatures that are higher by a few tens of percent. The use of a local background for the Fe/Si continuum fits naturally lowers the fit statistic per degree of freedom because the local background is less precisely determined than the standard background, but the actual fitted parameters are not much changed.

The faint c6a region southward of the knots in the A series is the most interesting of the Fe rich features. For this faint feature we show the fits using the local background only, as the off-source background gives statistically unacceptable fits. The spectrum is well-fitted with a model including only the elements Si and Fe (plus Ni), provided that the two elements have separate values of the ionization age. The temperature and ionization age of the Fe is similar to that obtained for the Fe-rich knots in Table 1, while the Si ionization age is similar to those obtained in Laming & Hwang (2003) for the O/Si knots. For this feature, we also performed a simultaneous fit of epoch 2000 and 2002 ACIS observations, allowing the two spectra to have different amounts of detector absorption according to their observation date. The parameters obtained are all very close to those obtained with the epoch 2000 observation alone, although with slightly smaller error ranges. Both sets of fits for the c6a region are shown in Figure 4, and the results summarized in Table 2. The Si and Fe ionization ages are not consistent with each other; from the error contours in Figure 4, their equality can be excluded at better than 99% confidence.

The line-to-continuum ratio images in Figure 1 show that the regions near c6a having very slight surface brightness enhancements over the background should have high Fe line strengths. We therefore extracted source and background spectra for this entire region by

specifying appropriate surface brightness cuts on the slightly smoothed image. The resulting background-subtracted spectrum can be fitted with a single component model including only Si and Fe (and Ni), but do not necessarily require Si and Fe to have separate ionization ages. An enhancement of the Fe abundance over Si at a level comparable to the Fe knots is indicated. Thus, while this entire region is indeed significantly Fe-enriched, as a whole it is not as pristine in Fe as is c6a. We have indeed examined a number of other features in this region, and while many of them show Fe enrichments of the order of the Fe knots, we have so far identified no others where the Fe is a pure as in c6a.

The Fe-rich knots considered here have Fe/Si abundance ratios that are typically an order of magnitude or more above the typical 0.25 ratio that is obtained through incomplete explosive Si-burning in a 20 $M_\odot$ progenitor (see Table 2 in Thielemann et al. 1996). It is clearly indicated that some of the Fe is produced with complete Si exhaustion, as is already well-established, both by earlier X-ray spectral observations (Hughes et al. 2000) and by the confirmed detection of the decay products of ^{44}Ti. The ^{44}Ti is formed in complete Si-burning that occurs at lower densities and is known as α-rich freeze out. The explicit identification of a possible pure cloud of Fe ejecta in region c6a suggests strongly that this may be one of the sites where α-rich freeze out occurred in Cas A.

4. Fe Ejecta Models and Discussion

In connection with Fe ejecta knots, it is necessary to consider that ^{56}Fe is originally formed as ^{56}Ni, which decays radioactively. If the initially formed Ni clumps are sufficiently large, they will be opaque to the γ ray radiation produced by the decays, and thereby expand to form a hot, low-density Fe bubble. As the reverse shock traverses these bubbles, the resulting turbulence plays an important role in mixing the Fe ejecta into overlying ejecta layers (Li, McCray, & Sunyaev 1993), as well as causing filamentation in the overlying (Si-rich) ejecta layers (Blondin, Borkowski & Reynolds 2001). The relative compactness of an Fe ejecta knot seen in the Type Ia (thermonuclear runaway) remnant of Tycho's supernova, caused Wang & Chevalier (2001) to suggest that the Fe in question is not ^{56}Fe, but rather ^{54}Fe, which is not formed by radioactive decays and is therefore not subject to the bubble effect. For core-collapse supernovae, and for Cas A in particular, this is a less satisfactory explanation because it is then difficult to produce a sufficient mass of ^{54}Fe, particularly if α-rich freeze out occurred during the explosion. On the other hand, if the ^{56}Ni clumps were sufficiently small at the outset, they could become optically thin to the γ-ray radiation sufficiently early that the bubble effect would be minimized.

We can demonstrate that the Fe knots we observe were indeed small enough to minimize

the bubble effect. The observed clump diameters of about 3″ give present day radii of 7.5×10^{16} cm at the 3.4 kpc distance of Cas A. Assuming that the radius increased proportionally to time, we get $r = 6 \times 10^{11}\ t_{\rm days}$ cm for the radius of a ^{56}Ni/^{56}Co clump at time $t_{\rm days}$ days after the explosion. The clump electron density varies as t^{-3} until interaction with the reverse shock, so extrapolating our $n = 7$ model back in time gives an electron density in the range $n_e = (1.5 - 3) \times 10^{14}/t_{\rm days}^3$ cm^{-3}. The optical depth to the center of the clump is then (Li, McCray, & Sunyaev 1993)

$$\tau\left(t_{\rm days}\right) \simeq \sigma n_e r \simeq \left(18 - 36\right)/t_{\rm days}^2, \tag{1}$$

where $\sigma = 0.31\sigma_{\rm T}$ for γ rays of energy about 1 MeV, and $\sigma_{\rm T}$ is the Thomson cross section. Hence we estimate that these clumps became optically thin ($\tau \sim 1$) to their own γ rays about 5 days after explosion. This is significantly shorter than the ^{56}Ni and ^{56}Co lifetimes of 8.8 and 111.3 days, respectively, so most of the radioactive energy is deposited outside the clump. We therefore do not expect the Fe knots we observe today to have undergone any type of bubble expansion.

We pursue a more quantitative interpretation of the Fe knots in Cas A than has been previously attempted, by calculating the variation of the electron temperature T_e with ionization age $n_e t$ for a variety of ejecta density profiles, as previously considered in Laming & Hwang (2003). We concentrate on models with an explosion energy of 2×10^{51} ergs, shocked ejecta mass $2M_\odot$, and circumstellar density $\rho r_b^2 = 14$ pc^2 cm^{-3}, with r_b the radius of the blast wave in pc. Laming & Hwang (2003) treated the case of pure O ejecta only; here we take compositions by mass of O:Si:Fe = 0.83:0.06:0.11 and Fe:Si = 0.9:0.1, which are approximately consistent with the spectral fits to the observed knots assuming an O-rich and Fe dominated composition for the continuum, respectively. These models are shown in Figures 4 and 5 as solid lines; the fit results are superposed as crosses for the "A" series of knots and, in Figure 5 only, as boxes for the diffuse Fe clouds, with the symbol size indicating the fit uncertainties in T_e and $n_e t$. Table 3 gives the ejecta mass coordinates inferred for each knot by matching the fitted value of $n_e t$ to the corresponding location in the ejecta for the hydrodynamic model. In this, we assume that the clumps have the same density as their surroundings. If overdense, the $n_e t$ we fit would correspond to a later reverse shock passage and hence place the knots further in in the ejecta; we estimate that a factor of three overdensity would lead to an overestimate of q by around 0.06. A similar underdensity would place the knots further out in the ejecta, by a similar amount. Following reverse shock passage, our Lagrangian plasma parcel likely undergoes interactions with secondary shocks while the reverse shock is relatively nearby, leading in any case to uncertainties in q of a similar magnitude.

The mass of ^{56}Fe contributed by the various knots is computed from the fitted emission

measure and element abundances of the knots in Table 3. Spherical geometries were assumed for the knots, and boxes for the diffuse features. The corresponding electron densities are also given in the table, and for comparison, the electron densities that are inferred from the models. The agreement between the observationally and theoretically inferred densities is generally within a factor of two, though it is somewhat worse for the larger East region. In any case, the observationally determined electron densities are systematically lower than the theoretically determined ones, which would seem to reinforce our assumption that the knots are not overdense.

According to the hydrodynamical model in Laming & Hwang (2003), the reverse shock is currently at an ejecta mass coordinate $q = 0.1 - 0.14$ for $n = 9 - 7$ models respectively. Hence the inner 10% of ejecta, i.e. the inner 0.2 $M_\odot$, has yet to encounter the reverse shock. Cas A is highly unlikely to have ejected more than 0.05 - 0.1 $M_\odot$ of ^{56}Ni (which β decays to ^{56}Fe), so the ^{56}Fe that we do see must have been mixed out into the envelope by Rayleigh-Taylor instabilities shortly after explosion. The estimated knot masses in Table 3 probably amount to a few percent of the total mass ejected, which is similar to the mass of ^{56}Ni inferred to have been mixed out into the envelope of SN 1987A (Pinto & Woosley 1988).

Kifonidis et al. (2000) and Kifonidis et al. (2003) have modelled core collapse explosions in two dimensions with the aim of following the propagation of metal clumps within the ejecta. For a Type II explosion of a 15 $M_\odot$ progenitor, Rayleigh-Taylor instabilities at the interfaces between the Ni+Si and O layers and the O+C and He layers produce clumps of widely varying element compositions. As the explosion proceeds, the reverse shock that is generated as the blast wave decelerates in the dense helium layer further shreds and mixes the clumps. The end result is that, at time 20,000 s after bounce, almost all the metals are completely mixed throughout the inner 3.4 $M_\odot$. The sole exceptions are those species like ^{44}Ti that are only synthesized in the innermost layers, and which remain correspondingly more localized. By contrast, a 15 $M_\odot$ progenitor that loses its outer envelope to a stellar wind before explosion as a Type Ib supernova has a much weaker reverse shock, with the result that metal clumps may survive and propagate further out into the ejecta. At time 3,000 s after bounce, ^{28}Si, ^{44}Ti and ^{56}Ni exist throughout the inner 2 $M_\odot$ (of an explosion progenitor of 5.1 $M_\odot$).

According to the mass coordinates we infer, the Fe clumps exist out to about 0.4 of the 2 $M_\odot$ ejecta, or 0.8 $M_\odot$. Adding 1.3 $M_\odot$ for the compact object mass, we arrive at $0.8 + 1.3 = 2.1$ $M_\odot$ for the observed outer extent of Ni mixing. This places the knots at a mass coordinate corresponding to the (Ni+Si)/O interface in a star that is initially of about 20 $M_\odot$ (Woosley & Weaver 1995). Though this is an appealing inference, it is necessary

to account for possible selection effects that determine the visibility of the knots. In the case of an O-rich composition for the knots, this apparent outer extent appears to be a real outer extent (see Figure 5). We expect that if higher $n_e t$ knots existed, we would be able to see them. For Fe-dominated composition, however, knots that encounter the reverse shock earlier than about 35 years after explosion (at ejecta mass coordinates $q_{\rm FeSi} \gtrsim 0.45$) will have cooled by radiative losses to temperatures below detectability as X-ray knots. In this case, the observed outer extent could be limited by this selection effect. We also fail to detect Fe knots with $n_e t \lesssim 10^{11}$ cm^{-3}s, i.e. in the inner 0.3 of the ejecta, or interior to 1.9 $M_\odot$ including the compact object. This might also be a selection effect caused by the rapid decrease in density as one move inwards into the ejecta. Fe that is deep in the ejecta may also be more likely to have created bubbles due to the radioactivity of its parent ^{56}Co nucleus, and so become even less dense than the O-rich ejecta that is assumed to surround it. The inferred mixing of the "c6a" and "east" regions out into regions that were originally O and are burnt to Si during the explosion is also consistent with the inference that ^{44}Ca found in SiC X grains is a decay product of ^{44}Ti formed in core collapse supernovae (e.g. Clayton et al. 2002).

It appears that the O:Si:Fe composition we infer can only be achieved by mixing products of complete Si burning with the products of O burning (to get Fe:Si right), and it is unlikely that a "knot" would survive such mixing as a distinct object. More plausible is the pure Fe:Si composition, that requires no further mixing after Si burning. Consequently the selection effect due to the radiative cooling of Fe rich knots discussed above is probably operative, and more Fe may exist at lower temperatures further out in the ejecta of Cas A.

5. Conclusions

Using Chandra observations combined with new modelling techniques, we have constrained the ejecta density profiles and Lagrangian mass coordinates of some of the Fe-rich knots in the southeastern region of Cas A. This makes it possible for the first time to compare observations in a quantitative manner with explosion models, and allows tests of nucleosynthesis and Rayleigh-Taylor instability in core collapse supernova explosions. The inference is that Fe and Si in knots are relatively uncontaminated by lower Z elements, and that their inferred ejecta mass coordinates appear to be entirely consistent with the expected Rayleigh-Taylor turbulence in a Type Ib supernova. We have further identified a region of nearly pure Fe ejecta that is a promising candidate for a site of α-rich freeze out. Again it is mixed out by Rayleigh-Taylor turbulence, but as a site α-rich freeze out associated with ^{44}Ti production, its origin should have been closer to the center and the mass cut than those

of the other Fe rich knots.

It is clearly desirable to make a complete census of the X-ray emitting Fe ejecta regions in Cas A and identify more regions that are highly enriched in Fe. For example, the ejected ^{44}Ti mass is estimated at $1.8 \times 10^{-4} M_{\odot}$ (Vink et al. 2001; Vink & Laming 2003), and 500-1000 times more ^{56}Ni by number is predicted globally from α-rich freeze out (Woosley & Hoffman 1991; Arnett 1996; Thielemann, Nomoto & Hashimoto 1996; The et al. 1998), so considerably more α-rich freeze out ashes should be present in Cas A to account for the ^{44}Ti emission than are inferred to be in regions "east" and "c6a". In this work we have principally been limited by the statistical quality of the current Chandra data sets when extracting spectra from the smallest possible spatial regions. A considerably deeper observation is required to take full advantage of the unprecedented spatial resolution available with Chandra, which appears to be crucial in studying the Fe emission and making progress on important issues in supernova physics such as asymmetries, nucleosynthesis and the location of the mass cut.

We wish to thank Larry Rudnick and Tracey Delaney for communication of their results prior to publication, and for allowing us access to their second epoch Chandra/ACIS data of Cas A prior to becoming public. JML was supported by basic research funds of the Office of Naval Research.

REFERENCES

Akiyama, S., Wheeler, J. C., Meier, D. L., & Lichenstadt, I. 2003, ApJ, 584, 954

Allende Prieto, C., Lambert, D. L., & Asplund, M. 2001, ApJ, 556, L63

Allende Prieto, C., Lambert, D. L., & Asplund, M. 2002, ApJ, 573, L137

Anders, E., & Grevesse, N. 1989, Geochim. Cosmochim. Acta, 53, 197

Arnett, D. 1996, Supernovae and Nucleosynthesis, (Princeton: Princeton University Press)

Blondin, J. M., Borkowski, K. J., & Reynolds, S. P. 2001, ApJ, 557, 782

Clayton, D. D., Meyer, B. S., The, L.-S., & El Eid, M. F. 2002, ApJ, 578, L83

DeLaney, T. A., & Rudnick, L. 2003, ApJ, in press, astro-ph/0303399

Gotthelf, E. V., Koralesky, B., Rudnick, L., Jones, T. W., Hwang, U., & Petre, R. 2001, ApJ552, L39

Grevesse, N., & Sauval, A. J. 1998, Space Science Reviews, 85, 161

Fryer, C. L., & Heger, A. 2000, ApJ, 541, 1033

Fryer, C. L., & Warren, M. S. 2002, ApJ, 574, L65

Fryer, C. L., & Warren, M. S. 2003, in preparation

Hughes, J. P., Rakowski, C. E., Burrows, D. N., & Slane, P. O. 2000, ApJ, 528, L109

Hwang, U., Holt, S. S., & Petre, R. 2000 ApJ, 537, L119

Iyudin, A. F., et al. 1994, A&A, 284, L1

Iyudin, A. F., Diehl, R.1, Lichti, G. G., et al. 1997, ESA SP-382, 37

Khokhlov, A., M., Höflich, P. A., Oran, E. S., Wheeler, J. C., Wang, L., & Chtchelkanova, A. Yu 1999, ApJ, 524, 107L

Kifonidis, K., Plewa, T., Janka, H.-T., & Müller, E. 2000, ApJ, 531, L123

Kifonidis, K., Plewa, T., Janka, H.-T., & Müller, E. 2003, A&A, submitted, astro-ph/0302239

Klein, R. I., McKee, C. F., & Colella, P. 1994, ApJ, 420, 213

Klein, R. I., Budil, K. S., Perry, T. S., & Bach, D. R. 2003, ApJ, 583, 245

Laming, J. M. 2001a, ApJ, 546, 1149

Laming, J. M. 2001b, ApJ, 563, 828

Laming, J. M., & Hwang, U. 2003, ApJ, submitted (Paper I)

Li, H., McCray, R., Sunyaev, R. A. 1993, ApJ, 419, 824

McKee, C. F., & Cowie, L. L. 1975, ApJ, 195, 715

Nagataki, S., Hashimoto, M., Sato, K., Yamada, S., & Mochizuki, Y. 1998, ApJ, 492, L45

Pinto, P. A., & Woosley, S. E. 1988, Nature, 333, 534

Poludnenko, A. Y., Frank, A., & Blackman, E. G. 2001, ApJ, 576, 832

Silver, E., et al. 2001, in AIP Conf. Proc. 587, Gamma Ray Astrophysics, ed. S. Ritz, N. Gehrels, & C. R. Shrader (Melville, NY:AIP), 860

The, L.-S., Clayton, D. D., Jin, L., & Meyer, B. S. 1998, ApJ, 504, 500

Thielemann, F.-K., Nomoto, K., & Hashimoto, M. 1996, ApJ, 460, 408

Timmes, F. X., Woosley, S. E., Hartmann, D. H., & Hoffman, R. D. 1996, ApJ, 464, 332

Vink, J., Kaastra, J. S., & Bleeker, J. A. M. 1996, A&A, 307, L41

Vink, J., Laming, J. M., Kaastra, J. S., Bleeker, J. A. M., Bloemen, H., & Oberlack, U. 2001, ApJ, 560, L79

Vink, J., & Laming, J. M. 2003, ApJ, 584, 758

Wang, C.-Y., & Chevalier, R. A. 2001, ApJ, 549, 1119

Willingale, R., Bleeker, J. A. M., van der Heyden, K. J & Kaastra, J. S. 2002, A&A, 381, 1039

Woosley, S. E., & Hoffman, R. D. 1991, ApJ, 368, L31

Woosely, S. E., & Weaver, T. A. 1995, ApJS, 101, 181

Table 1. Fits to Fe-rich Knots

Knot:[a]	A10	A11	A12	A13	A14	A15	A16	A17
				Abundances relative to O, standard background				
k_BT_e[b]	2.11	2.13	1.57	2.03	1.79	1.58	1.98	1.99
(keV)	1.80-2.52	1.76-2.59	1.50-1.67	1.40-2.45	1.58-2.07	1.46-1.87	1.71-2.26	1.86-2.25
n_et	1.98	2.32	7.92	0.92	2.28	2.19	0.97	1.63
(10^{11} cm^{-3}s)	1.48-3.07	1.45-3.21	4.98-11.7	8.63e+10-1.90	1.65-3.72	1.74-2.90	7.57e+10-1.15	1.58-2.05
Mg	0.007	0.075	0	0.085	0	0.043	0.018	0.013
	< 0.20	<0.13	<0.20	0.056-0.15	<0.075	0.023-0.095	<0.049	< 0.049
Si[c]	0.40	0.29	1.34	0.38	0.32	0.13	0.14	0.076
	0.29-0.85	0.23-0.57	0.59-2.48	0.26-0.48	0.22-0.49	0.094-0.19	0.12-0.18	0.066-0.084
S	0.43	0.30	0.97	0.34	0.28	0.17	0.14	0.072
	0.30-0.91	0.22-0.46	0.44-3.20	0.26-0.39	0.18-0.40	0.12-0.20	0.11-0.17	0.051-0.093
Ca	0.64	0.53	2.41	0.49	0.70	0.50	0.48	0
	0.21-1.07	0.27-0.68	1.50-3.11	0.11-0.85	0.28-1.13	0.18-0.83	0.16-0.79	< 0.074
Fe	1.29	0.72	2.67	0.28	1.09	0.25	0.25	0.26
	0.84-3.20	0.50-1.83	1.30-20.4	0.14-0.35	0.74-1.98	0.17-0.44	0.20-0.34	0.22-0.29
n_H	1.33	1.27	1.37	1.16	1.42	1.17	1.20	1.18
(10^{22} cm^{-2})	1.19-1.39	1.17-1.40	1.33-1.40	1.05-1.20	1.35-1.48	1.03-1.38	1.12-1.29	1.05-1.26
EM (10^{11} cm^{-5})	2.25	4.68	1.69	3.23	2.88	4.39	4.26	6.86
χ^2	116.4	218.2	180.0	157.3	129.9	78.2	135.1	146.7
χ^2/dof	1.25	1.93	1.70	1.69	1.44	0.98	1.54	1.47
# dof	93	113	106	93	90	80	88	100
# cts	5221	6748	5541	4679	5123	3702	4396	5416
				Abundances relative to Si, standard background				
k_BT_e[b]	1.73	1.59	1.56	1.23	1.50	1.32	1.20	1.47
(keV)	1.65-1.84		1.48-1.61		1.42-1.57	1.32-1.40		
n_et	3.69	7.55	10.1	4.56	5.59	10.9	9.57	7.61
(10^{11} cm^{-3}s)	3.41-5.48		>7.73		4.12-8.27	5.89-16.4		
Fe	3.55	2.84	1.91	1.43	3.67	2.25	2.10	3.85
	3.05-3.74		1.54-2.19		3.30-4.10	1.95-2.83		
n_H	1.44	1.53	1.41	1.66	1.53	1.49	1.50	1.48
(10^{22} cm^{-2})	1.35-1.49		1.36-1.49	1.50-1.60	1.33-1.60			
χ^2	124.0	236.3	182.2	227.2	145.5	134.8	236.6	243.4
χ^2/dof	1.32	2.07	1.70	2.42	1.60	1.66	2.66	2.41
# dof	94	114	107	94	91	81	89	101
				Abundances relative to Si, local background				
k_BT_e[b]	1.77	1.68	1.58	1.24	1.52	1.34	1.20	1.47
(keV)	1.63-1.95	1.60-1.78	1.52-1.69	1.07-1.92	1.46-1.62	1.29-1.36		
n_et	3.65	7.40	1.02e+12	3.41	5.33	8.33	9.58	7.97
(10^{11} cm^{-3}s)	2.83-5.26	5.30-10.0	>6.85	1.60-5.58	3.75-6.80	6.18-14.7		
Fe	3.84	2.76	1.95	0.39	3.93	2.57	2.10	3.89
	3.27-4.38	2.32-3.38	1.52-2.28	0.28-0.49	3.50-4.58	1.66-2.97		
n_H	1.44	1.45	1.42	0.93	1.54	1.53	1.50	1.48

Table 1—Continued

Knot:[a]	A10	A11	A12	A13	A14	A15	A16	A17
(10^{22} cm^{-2})	1.33-1.50	1.34-1.52	1.38-1.49	0.69-1.23	1.47-1.60	1.35-1.54		
χ^2	109.4	218.1	170.6	179.3	124.8	111.2	210.3	209.1
χ^2/dof	1.16	1.91	1.59	1.91	1.37	1.37	2.36	2.07
# dof	94	114	107	94	91	81	89	101

[a]Knots are numbered moving out to the limb, continuing the east radial series in Paper I. Errors quoted are 90% confidence when the $\chi^2/dof < 2.0$.

[b]Electron temperature in keV. Uncertainties are typically ±0.1 keV.

[c]Element abundance ratio by number relative to solar values of Anders & Grevesse (1989). Note that these are superseded by Grevesse & Sauval (1998), Allende Prieto, Lambert, & Asplund (2001), and Allende Prieto, Lambert, & Asplund (2002). In particular abundances relative to O increase by 1.75.

Table 2. Fits to Diffuse Regions

Region:	c6a	c6a (joint)	East
$k_B T_e$[a]	2.06	1.90	2.59
(keV)	1.88-2.30	1.80-1.97	2.09-2.97
$n_e t_{Si}$	0.74	0.80	1.59
(10^{11} cm^{-3}s)	0.187-1.71	0.421-1.30	1.26-2.32
S[b]	0	0	0.72
	...	...	0.55-0.90
Ar	0	0	2.15
	...	...	1.16-3.16
Fe	22.8	20.0	5.77
	16.1-49.4	14.1-27.1	5.43-6.78
$n_e t_{Fe}$	3.3	3.81	...
(10^{11} cm^{-3}s)	2.5-4.0	3.32-4.90	...
n_H	1.34	1.41	1.27
(10^{22} cm^{-2})	1.27-1.43	1.35-1.47	1.23-1.31
EM (cm^{-5})	1.54e+10	1.89e+10	1.60e+11
χ^2	110.3	262.7	244.8
χ^2/dof	1.33	1.45	1.56
# dof	83	181	157
# cnts[c]	5668 (60%)	5773+5608 (60%)	27816 (57%)
Region Size			

[a]Electron temperature in keV. Uncertainties are typically ±0.1 keV.

[b]Abundance by number relative to Si at the solar value.

[c]Quantity in parentheses is the fraction of the counts remaining after background subtraction.

Table 3. Ejecta knot abundances and mass coordinates

Region	$q_{\rm OSiFe}$[a]	$q_{\rm FeSi}$[b]	Fe masses[c]	Obs. n_e[d]	Model n_e[e]
A10	0.32-0.37	0.35-0.39	7e-5	12	12-20
A11	0.32-0.37	0.39-0.44	8e-5	13	20-39
A12	0.38-0.44	> 0.41	9e-5	15	> 26
A13	0.29-0.34	0.31-0.38	4e-5	7	7-18
A14	0.31-0.36	0.37-0.41	8e-5	12	16-26
A15	0.31-0.34	0.40-0.46	4e-5	7	23-50
c6a	-	0.36-0.38	2e-4	8	14-18
East	-	0.31-0.34	$\sim$1e-3	2	7-11

[a]Ejecta mass coordinate for OSiFe composition, assuming no over/under density.

[b]Ejecta mass coordinate for FeSi composition, assuming no over/under density.

[c]Fe masses computed from fitted emission measures and Fe abundances assuming pure Fe, and spherical knots of 1.75″ radius, except for c6a (3.8″ × 8.8″ box) and East (11″ × 24″).

[d]Electron densities in $\rm cm^{-3}$ from emission measure and fitted abundances.

[e]Electron densities in $\rm cm^{-3}$ from $n = 7$ model corresponding to the range in $q_{\rm FeSi}$.

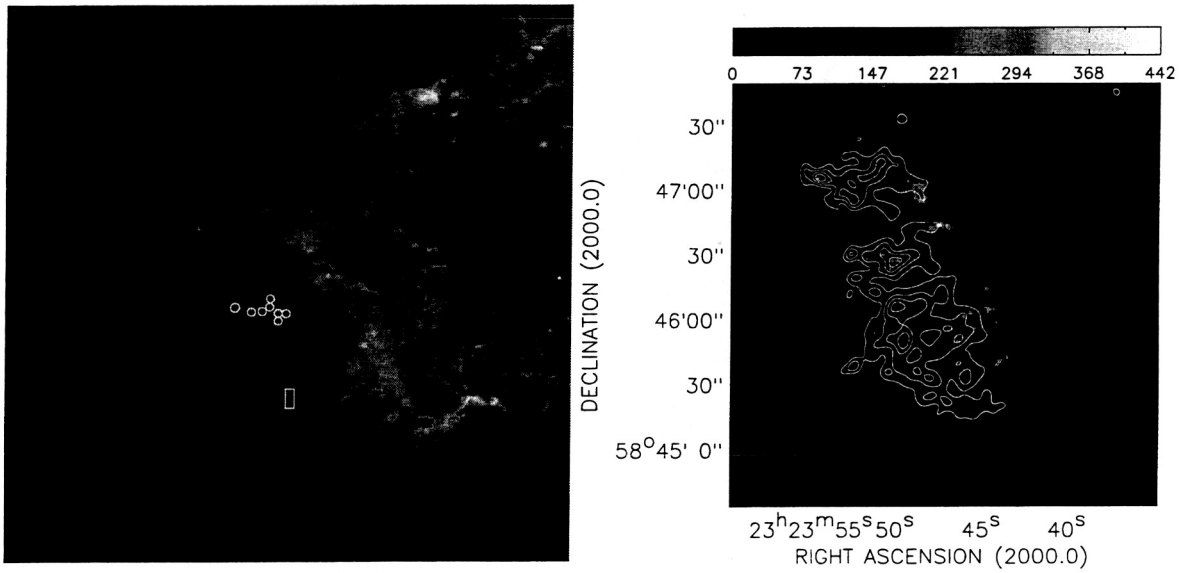

Fig. 1.— Detail of the southeastern region of Cas A as imaged by the Chandra X-ray Observatory in January 2000. The spectral extraction regions used for the linear series of compact Fe-rich knots (circles, starting from the center moving outwards) and the extremely Fe-rich cloud (box) are marked. On the right is the Chandra image including only the photons in the Fe L energy range; superposed are contours showing Fe L line-to-continuum ratios.

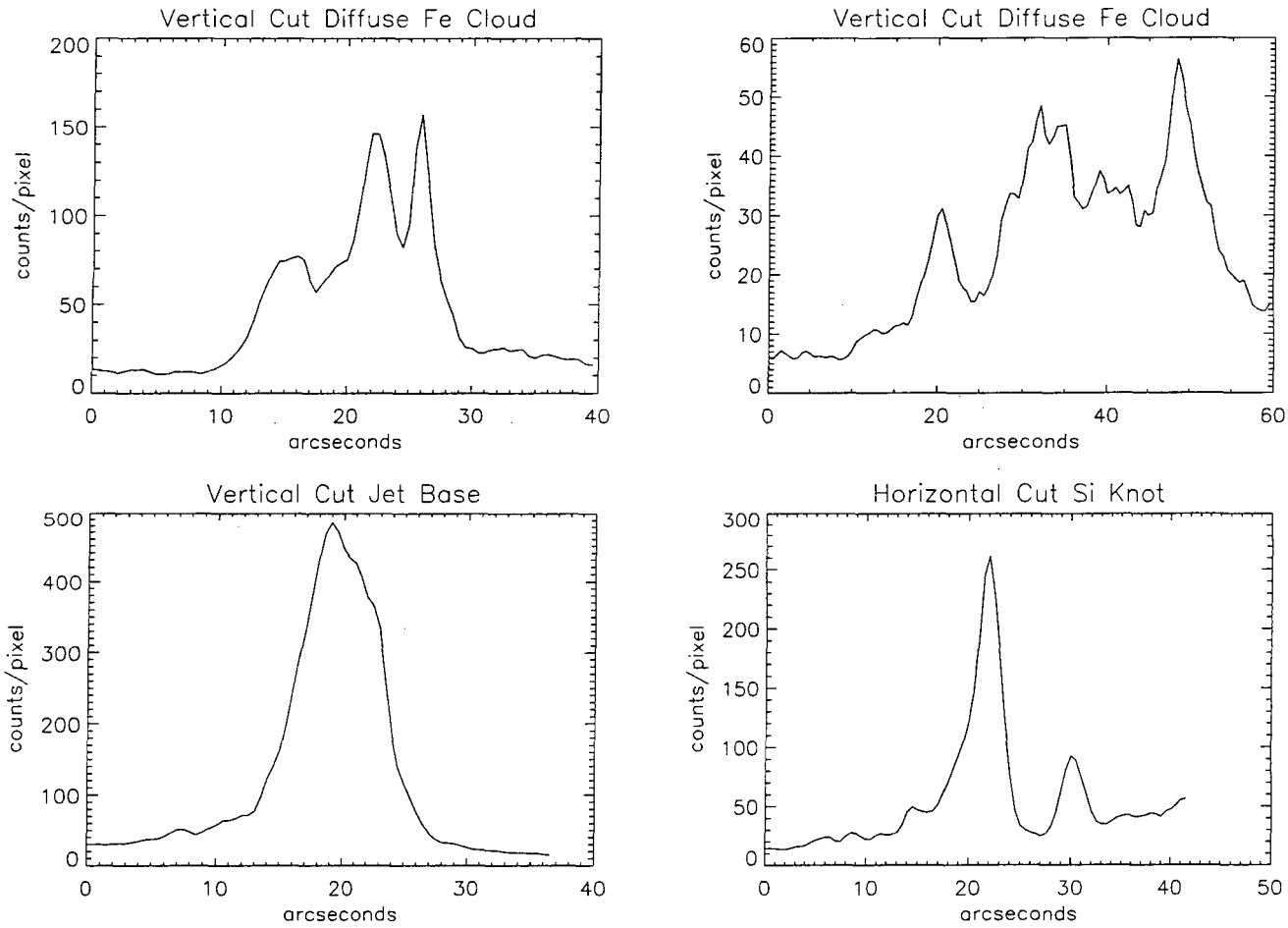

Fig. 2.— Crosswise cuts across various features show the relative surface brightness contrast. Plotted are the average counts per pixel across (a) a 3″-wide vertical strip through Fe-rich knots 13 and 14 (b) a 4″-wide vertical strip passing through the very Fe-rich diffuse cloud (c) a 6″-wide vertical strip through the base of the jet, analyzed in Paper I (d) a 3″-wide horizontal strip through an isolated Si-rich knot.

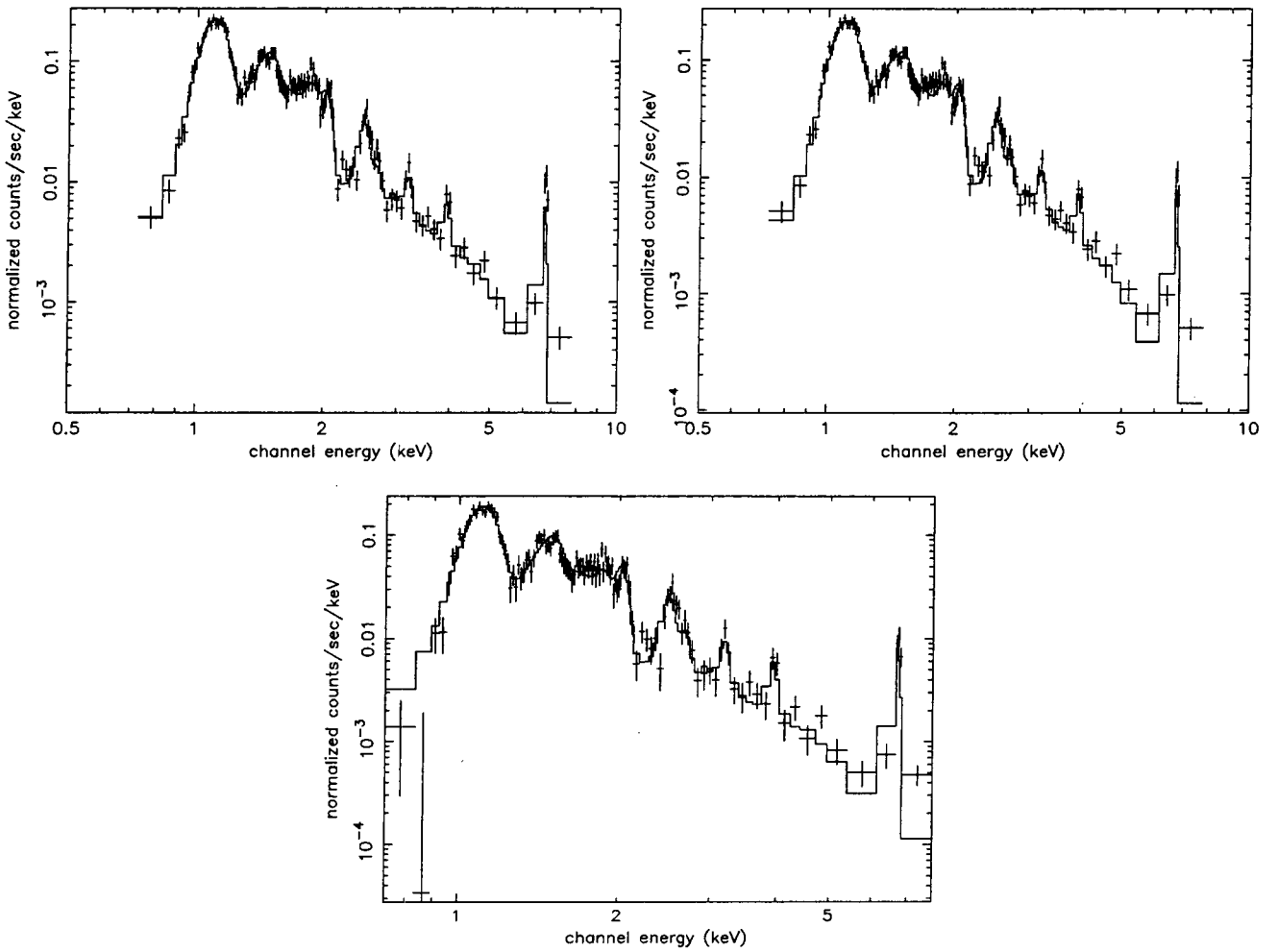

Fig. 3.— Chandra ACIS spectra of a representative Fe-rich knot in the eastern radial series, fitted with a single temperature, single ionization age model with O continuum (left) and Si continuum (right) and the standard off-source background spectrum. In the lower panel, the same knot is fitted with a Si continuum model with a local background.

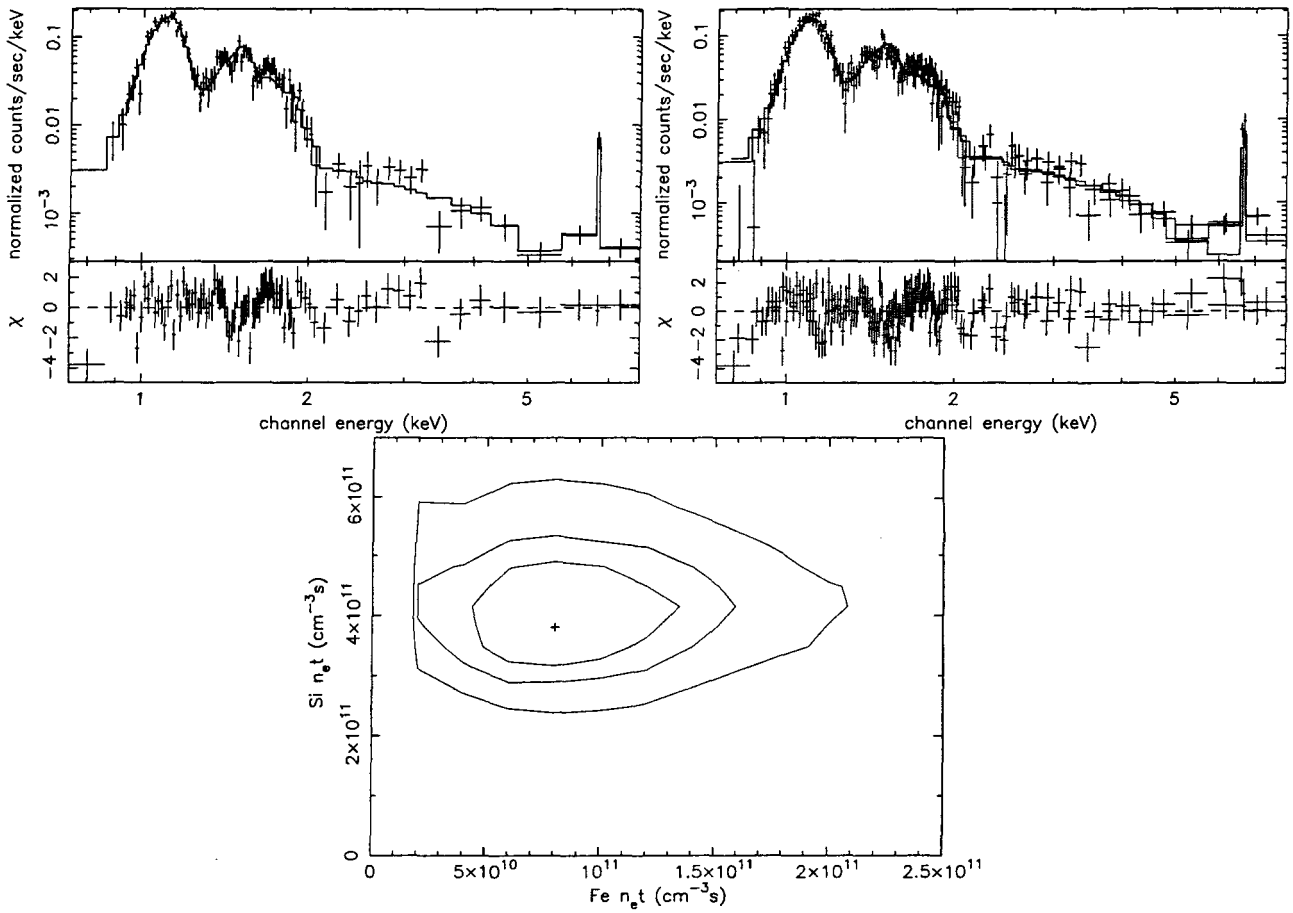

Fig. 4.— (Upper) The 2000 epoch ACIS spectrum of the diffuse Fe cloud is shown with a single temperature model with separate ionization ages for Si compared to Fe and Ni (no other elements are included) in the left panel; the jointly fitted 2000 (red) and 2002 (black) epoch spectra for the Fe cloud are shown in the right panel. (Lower) Confidence contours for Si and Fe ionization ages showing $\Delta\chi^2$=2.3,4.6,9.2 for the joint fit shown above.

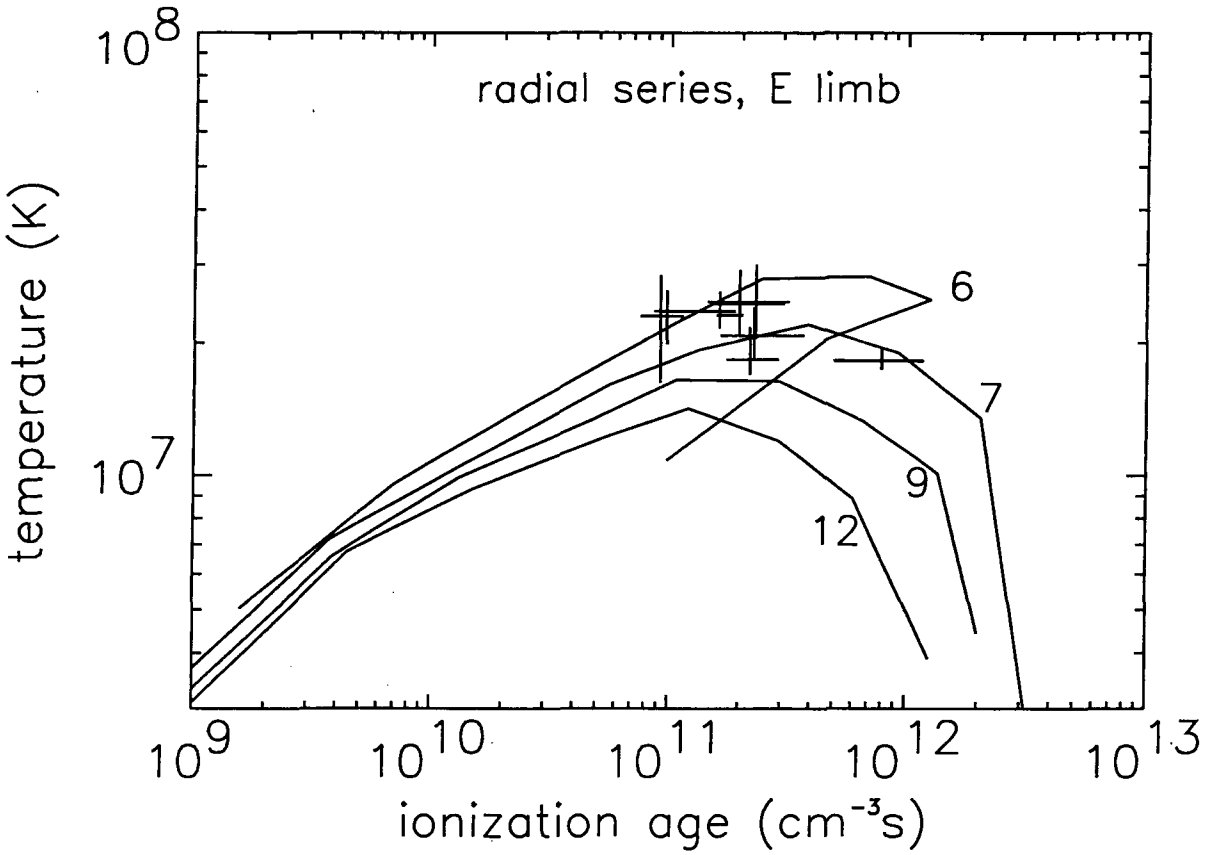

Fig. 5.— Plots of T_e against $n_e t$ for varying ejecta envelope power-law slopes, for a composition O:Si:Fe of 0.83:0.06:0.11 by mass. Data points from the fits to the "A" series of knots are plotted as crosses, with the size of the cross indicating the fit uncertainties. The point at highest $n_e t$ for $n = 6$ corresponds to ejecta at the core-envelope boundary. For higher values of n this plasma undergoes thermal instability.

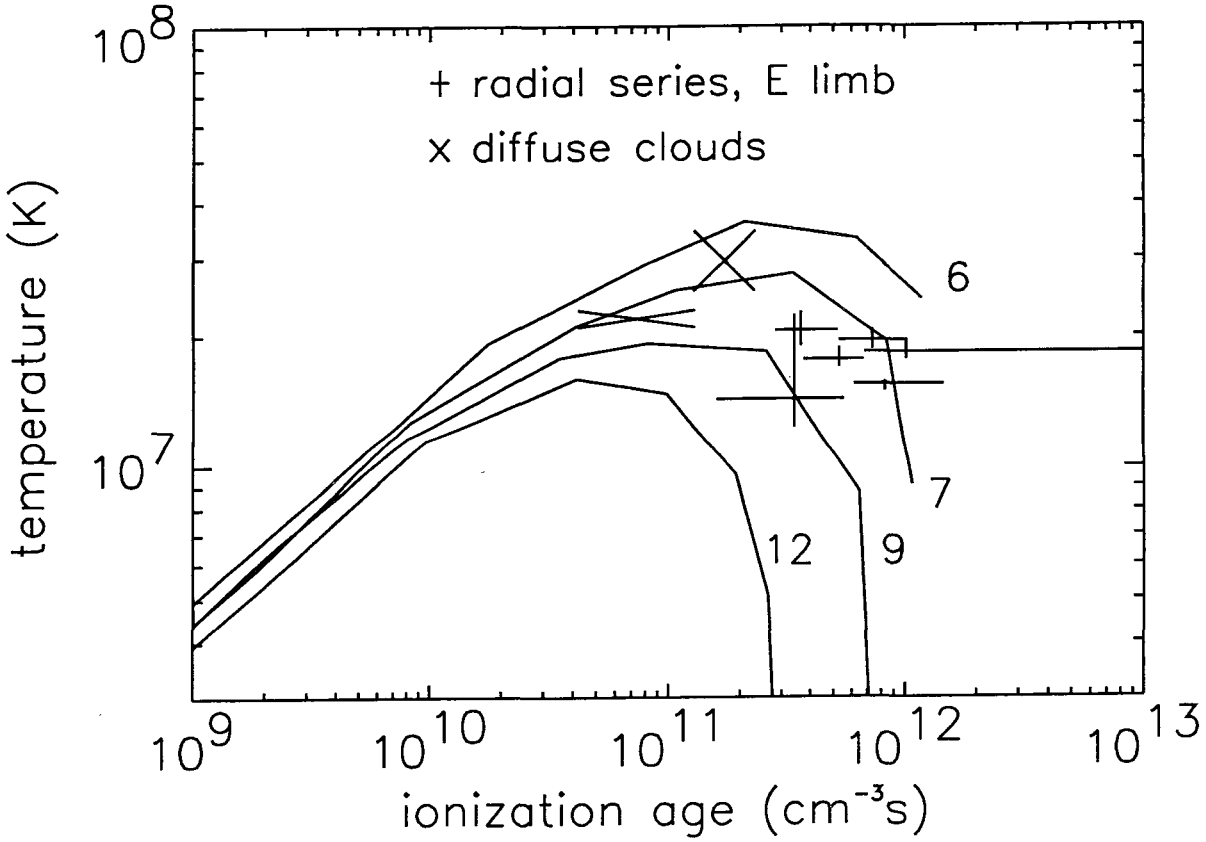

Fig. 6.— Plots of T_e against $n_e t$ for varying ejecta envelope power-law slopes, for a composition Si:Fe of 0.1:0.9 by mass. Data points from the fits to the "A" series of knots are plotted as crosses, with the size of the cross indicating the fit uncertainties. The "diffuse Fe clouds" are plotted as boxes, again with size indicating uncertainties.